Operando study of Ni-22Cr oxidation dynamics with nanoscale resolution in an X-ray photoemission electron microscope

Keithen G. Orson [a], William H. Blades [a,b], Anna Costine [a], Zachary D. Harris [c], Yuran Niu [d], Alexei Zakharov [d], Petra Reinke [a,*]

[a] Department of Materials Science and Engineering, University of Virginia, Charlottesville, VA 22904, USA
[b] Department of Physics and Engineering Physics, Juniata College, Huntingdon, PA 16652, USA
[c] Department of Mechanical Engineering and Materials Science, University of Pittsburgh, Pittsburgh, PA 15261, USA
[d] MAX IV Laboratory, Lund University, Sweden

ABSTRACT

Understanding the initial oxidation pathways on binary Ni-Cr surfaces is import for alloy development and rational design. The early-stage oxidation of Ni-22wt% Cr is studied in-situ and in-operando with synchrotron-based x-ray photoelectron microscopy (XPEEM) and x-ray photoelectron spectroscopy (XPS) at 500 °C and oxygen exposure from 0 to 65 Langmuir. Preferential Cr oxidation is accompanied by Cr depletion in the alloy. Analysis of XPEEM timeseries and hyperspectral datasets presented the combined challenge of large datasets and varying image background. Hyperspectral data was approached using a combination of data dimensionality reduction techniques including principal component analysis (PCA), non-negative matrix approximation (NNMA), cosine similarity (CS), and tiling. These methods deliver spatially resolved chemical identification and extract the evolution of oxide island distribution over time. XPEEM timeseries thresholding shows that chromia islands are embedded in a thinner layer of oxidic Cr components, and larger islands emerge at ~30 L. Their growth rate and size distribution differs markedly for (104) and (212) surfaces studied here. The layer-plus-island growth mode is reminiscent of a Stranski-Krastanov type growth and increases the oxide layer heterogeneity. This work demonstrates a local-background framework for island identification and the utility of PCA, NNMA, and cosine similarity for analysis of XPEEM datasets.

1. Introduction

Ni-Cr alloys are classified as superalloys and resist oxidation due to the formation of a stable oxide layer that limits internal oxidation at high temperatures and promotes passivity in aqueous corrosion.[1–4] The initial stage of oxidation where the Ni-Cr alloy surface is transformed to an oxide establishes the conditions for the subsequent steady-state behavior.[1] Recently there has been a significant experimental thrust to understand the early oxidation stages at the surface at different temperatures and oxygen exposures.[5–9] The pursuit of a comprehensive understanding of the chemical, structural, thermodynamic and kinetic factors which control these initial reaction steps is therefore highly relevant. The study presented here closes a gap in understanding of early oxidation[10,11] by using operando experiments that access the time evolution of the oxide from alloy to thin oxide layer. The initial oxidation process is accessible using surface science

experimental methods, many of which were developed to study crystal growth, and catalytic reactions. The focus of the present work is the use operando x-ray photoemission electron microscopy (XPEEM) to observe the alloy transformation during the initial steps of oxide formation.

The competition between Ni and Cr oxide formation is one of the central questions in binary Ni-Cr oxidation studies.[11] For alloy design, a critical concentration limit of the passivating element(s) in the alloy, which forms the desired protective oxide (Cr_2O_3 for Ni-Cr alloys), is empirically targeted. Above this limit, the protective oxide forms a closed layer and thus performs as intended. For the Ni-Cr alloy the critical Cr concentration is about 14–16 wt% for thermal oxidation, and the work here uses a Ni-22wt%Cr alloy that is well above this limit.[12,13] Oxidation of the pristine Ni-Cr alloy surface proceeds from adsorption of oxygen, where surface reconstructions can occur. After adsorption of oxygen at the surface, the growth of 2D oxides (surface oxides) commences and is followed by 3D growth of oxide nodules and

islands. Thermodynamically, the formation of Cr_2O_3 is preferred over NiO but kinetic factors such as epitaxial growth and limited transport of Cr through the alloy, can promote NiO. For example, NiO preferentially and rapidly nucleates at step edges because of epitaxial matching at the interface.[6,14,15] For temperatures below ~700 °C the Cr diffusion from the bulk is limited,[1,16] but recent work by Larsson et al.[17] shows that for temperatures > 400 °C[16] the Cr_2O_3 contributions to the oxide increase significantly in the early stages of growth. A recent low-temperature (200 °C) oxidation study by Volders et al.[10] illustrates the severely diffusion-limited case where only Cr from very few atomic layers is available for oxide formation.

Additionally, Ni-Cr based superalloys display good aqueous corrosion performance and are resistant to breakdown in chemically aggressive environments, such as salt water. The primary passivation of binary alloys in aqueous environments follows different reaction pathways, [18] but many alloy characteristics such as alloy composition, critical Cr concentration, and the surface orientation influence the passivity of the oxides and hydroxides that form at the surface.[19,20] The nature of the early-stage passive film that forms on Ni-Cr alloys is complex and further improvements can be achieved by adding minor alloying elements specifically Mo and W.[3,19,20] Accordingly, binary Ni-Cr alloys have emerged as model systems for building a comprehensive understanding of the early stages of oxidation and corrosion.[10,11,21,22] These studies highlight the important role that Ni-Cr based superalloys have in assisting the oxidation and corrosion communities in building a complete understanding of the protective oxides that grow at their surfaces.

The initial steps of oxidation can be framed using models developed for thin-film nucleation and growth.[4,6,23] The interplay between surface and interfacial energies, strain, diffusion, Ehrlich-Schwoebel barriers, and nucleation processes define the respective growth modes such as island (Frank-van der Merwe), island-layer (Stranski-Krastanov), and layer-by-layer (Vollmer-Weber) growth modes. [24,25] The continued growth, once a complete oxide layer is present, can generally be described by Mott-Cabrera then Wagner kinetics connected to the point defect model.[1,26] Adding complexity is the possibility of sub-surface nucleation of oxide on the more open surfaces where oxygen atoms can reach higher coordinated sub-surface sites.[23] It is expected that the crystallographic orientation of the Ni-Cr alloy influences the oxide formation and performance, which has been shown in a comparison of Ni-Cr(100) and (111) by Blades et al.,[6,8] and experiments in aqueous corrosion by Gusieva et al.[19] The varied nature of interfaces in aqueous passive films, which can be crystalline and epitaxial[27,28] or disordered,[29] makes it difficult to quantify and understand the role of crystallographic orientation in this context. With respect to high-temperature oxidation, Ni(100) and Ni-Cr(100)[7] oxidation is particularly interesting since it relates the initial adsorption reaction to oxide nucleation via a surface reconstruction: The pure Ni(100) surface adopts a c(2×2)-O surface reconstruction which initiates step edge faceting, and reduces the nucleation sites for NiO causing delayed nucleation kinetics.[7,30–33] The addition of Cr disrupts this reconstruction on Ni-Cr (100)[34] and removes the kinetic limitation leading to rapid NiO growth.

To date, much of the experimental data gathered on early-stage oxidation use x-ray photoelectron spectroscopy (XPS)[35,36] and x-ray absorption spectroscopy (XAS) to unravel the chemistry and bonding, and scanning tunneling microscopy (STM) and spectroscopy (STS) as a local probe for topography and electronic structure.[3,5,9,37] Operando and in-situ investigations are gaining in importance and add information on the oxide evolution such as the operando TEM studies by Luo et al. [37] and deoxidation of steel by Zhu et al.[38] High resolution probes of early oxidation have uncovered not only details on the oxide growth,[7,36] highlighting deviation from known models,[39] but also showed significant nanoscale heterogeneities including islands during oxidation ranging from 450 to 1100C.[15,22,40,41] Specifically, the local Cr distribution that evolves during early-stage growth is proposed to impact the steady-state growth of the oxide layer.[42] A

comprehensive understanding of these initial reaction steps is pursued using synchrotron-based XPEEM. XPEEM has also been used to study thin film growth,[43] oxidation and deoxidation of stainless steel,[38, 44–46] and early oxidation of Ni(111) surfaces.[39] The study presented here closes the gap in understanding of how the early oxide evolves using *operando* surface-science methods. XPEEM offers unique insight in the early stages of oxidation by combining high spatial resolution with local chemical information and near-video rate monitoring of surface processes.

Moving past single-crystal to real-world polycrystalline systems helps explain the role of crystallographic orientation and the impact of grain boundaries on initial oxidation. The work presented here leverages *operando* XPEEM to observe the alloy to oxide transformation simultaneously on two grain surfaces with different crystallographic orientation. This work is complemented by *in situ* XPS measurements, and development of image analysis and processing code specifically for XPEEM datasets. Complementary XPS studies confirm the exclusive formation of chromia. The Cr content in the alloy is above the critical limit for a Cr-dominated oxide, and Cr diffusion from the bulk is not yet a limiting factor at these exposures and temperatures. Results from data dimensionality reduction in combination with the cosine similarity deliver quantitative chemical information for each pixel and enable reliable thresholding for measuring nucleation densities. The new combination of data analysis and experimental techniques enables tracking of the oxide layer growth in operando. The oxidation progression begins with the formation of an oxygen adsorbate and a thin oxidic layer, followed by the emergence of well-defined chromia islands. This is reminiscent of a combined layer-island growth mode,[23] and the density, spatial and size distribution of the chromia islands differs between the two surfaces. [23]

2. Experimental

Herein the oxidation of polycrystalline Ni-22Cr and the emergence of oxide islands is studied using XAS (X-ray absorption spectroscopy) and photoelectron valence band spectroscopy (VB-PEEM). Individual grains in the alloys are identified prior to the XPEEM experiment using EBSD (electron backscatter diffraction) and the crystallographic orientation is confirmed with LEEM (low energy electron microscopy). In this work two grains with (104) and (212) surfaces and the grain boundary between them are observed. The oxidation is performed at 500C and pressure of p(O_2)= 7.5×10^{-9} Torr with an exposure steps up to a total exposure of 65 Langmuir, which allows for direct observation of the oxidation process. A Langmuir (L) is a unit of exposure and corresponds to exposure for the time of 1 s at a pressure of 10^{-6} Torr. The resulting datasets include hyperspectral XAS maps and time-series images. For the time series study, tools are developed to mitigate uneven illumination within the field of view and to segment the oxide islands. The hyperspectral images are interrogated with data dimensionality reduction techniques principal component analysis (PCA) and non-negative matrix approximation (NNMA).

Alloy Preparation: The alloy sample with Ni-22wt%Cr composition was arc-melted, cast, cold rolled, solutionized at 1300 °C for 1 h, recrystallized at 800 °C for 48 h, then sectioned. The polycrystalline Ni-22wt%Cr alloy sample was subsequently annealed for 150 h at 1150C to increase the grain size while retaining a single-phase FCC alloy. Specimens were polished with SiC grinding paper, then a diamond slurry, and finished with 0.05 mm colloidal silica. Fiducial markers were placed on each sample using a Vickers microhardness indenter. For the sake of brevity, Ni-22Cr is used to denote the alloy composition moving forward.

Alloy Characterization: The orientation of the grains was characterized via electron backscatter diffraction (EBSD) using an FEI Helios G4 UC dual-beam scanning electron microscope equipped with an Oxford Instruments Symmetry camera. A 3 × 3 montage of EBSD scans were performed on each specimen at a magnification of 50 × using step sizes

between 5 and 10 μm, an accelerating voltage of 20 keV, and probe current of 3.2 nA. Inverse pole figure maps for each scan were calculated using the Oxford Aztec software. The location of the XPEEM experiment section, as shown in Fig. 1, was identified through comparison with the EBSD map: images with successively smaller magnification in MEM (mirror electron microscopy) mode in the XPEEM were matched to features of the grain boundary, shape of adjacent grains, and position of fiducial markers in the EBSD map. In addition to the grain boundary, a few polishing grooves are still visible in the XPEEM image. From the EBSD measurements the orientation of the grains can be assigned as following: the top grain surface is the (212) plane, and the bottom grain surface is the (104) plane. Their orientation was confirmed with LEEM (low energy electron diffraction microscopy). Fig. 1 also shows structural models of the (212) and (104) surfaces, which include terraces with a width of 0.74 nm and 0.70 nm, respectively.

XPEEM Experiment and Sample Preparation: The Ni-22Cr sample was studied at the MAXPEEM endstation at the MAX IV synchrotron facility (Lund, Sweden) with an optimal X-ray spot size of 20–30 μm.[47] The experiment is conducted with an Elmitec III LEEM.[47,48] The sample was introduced to the preparation chamber with a base pressure of 1.2×10^{-10} Torr. The native oxide was removed by annealing for 1.25 h at 600 ℃ and flash annealing for 10 s at 700–800 ℃ for 18 cycles. Cleanliness of the surface was confirmed with XPS (x-ray photoelectron spectroscopy) in the XPEEM setup, and only traces of oxygen remained.

Oxidation Conditions The total oxidation with 65 Langmuir (L) exposure to oxygen was conducted on the clean alloy surface at 500 ℃ and was divided into three time series videos which show the evolution of the surface oxide at $p(O_2) = 7.5 \times 10^{-9}$ Torr.[49] The oxidation conditions for the operando experiments are: 1st oxidation: + 5 L (11 min) of exposure; 2nd oxidation: + 15 L (33 min) for a total of 20 L of exposure; 3rd oxidation + 45 L (99 min) for a total exposure of 65 L. In between the time series hyperspectral images of the L-edge for Ni and Cr were recorded and deliver two distinct set of data: (a) in-situ *hyperspectral* images, and (b) *operando* single-energy time series.

XPEEM Datasets: XPEEM was used to record the evolution of the surface in *operando* by monitoring the Cr L3-edge at a single energy of 577.5 eV with μ-XAS (x-ray absorption) measured using energy-filtered secondary electron yield.[47] This energy is positioned on the Cr_2O_3 peak within the Cr L-edge which also includes contributions from the metal Cr(0). The single energy time series delivered a total of 952 images, each capturing 8.63 seconds, which corresponds to approximately 0.07 L of exposure per image. A photon energy of 577.5 eV at the Cr L3-edge was used since it aligns with the Cr_2O_3 feature; no such distinct peak is available on the Ni L3-edge. μ-XAS *hyperspectral maps* where each pixel corresponds to a single XAS spectrum, were recorded for the Cr- as well as the Ni L-edge. Valence band spectra (VB-PEEM) were measured in photoemission mode with a photon energy of 100 eV. The hyperspectral maps were recorded at 5, 20 and 65 L of exposure for the L-edge, and the valence band (VB) spectra hyperspectral images were measured at 20 and 65 L exposure. The probing depth of XAS for Cr is between 5 and 15 nm [50] and in the valence band spectra only the top 1–2 nm of the surface is probed. The spatial resolution was 25 nm per pixel for 1024×1024 pixel images (corresponding to 2×2 detector binning) and 50 nm per pixel for 512×512 pixel (corresponding to 4×4 detector binning) images covering a total area of 25.6×25.6 μm^2.

XPS - Replica Experiment: The oxidation experiment was replicated in a laboratory XPS system using the same sample, sample preparation protocols and oxidation conditions. This affords quantitative information about elemental concentrations and chemical species in alloy and oxide. The XPS instrument is a Scienta Omicron Multiprobe MXPS with a monochromatic Al-K$_\alpha$ x-ray source (hν = 1486.7 eV) and core levels were recorded with a pass energy of 20 eV and step size of 0.05 eV. The instrument was calibrated using Au 4 f$_{7/2}$ at 84.0 eV. The O 1 s, C 1 s, Ni 2p$_{3/2}$, and Cr 2p$_{3/2}$ peaks were measured before oxidation, after 20 L, and after 65 L of oxidation at $p(O_2) = 7.5 \times 10^{-9}$ Torr. The XPS measurement area is on the order of 1 mm^2 and therefore averages over several grains.

2.1. Data analysis

Fig. 2 includes a flow chart summarizing the image-analysis process from data acquisition to interpretable datasets. The analysis is split into two branches: the in-situ, μ-XAS hyperspectral images (Fig. 2.A) and the operando single energy time series (Fig. 2.B). The time series were
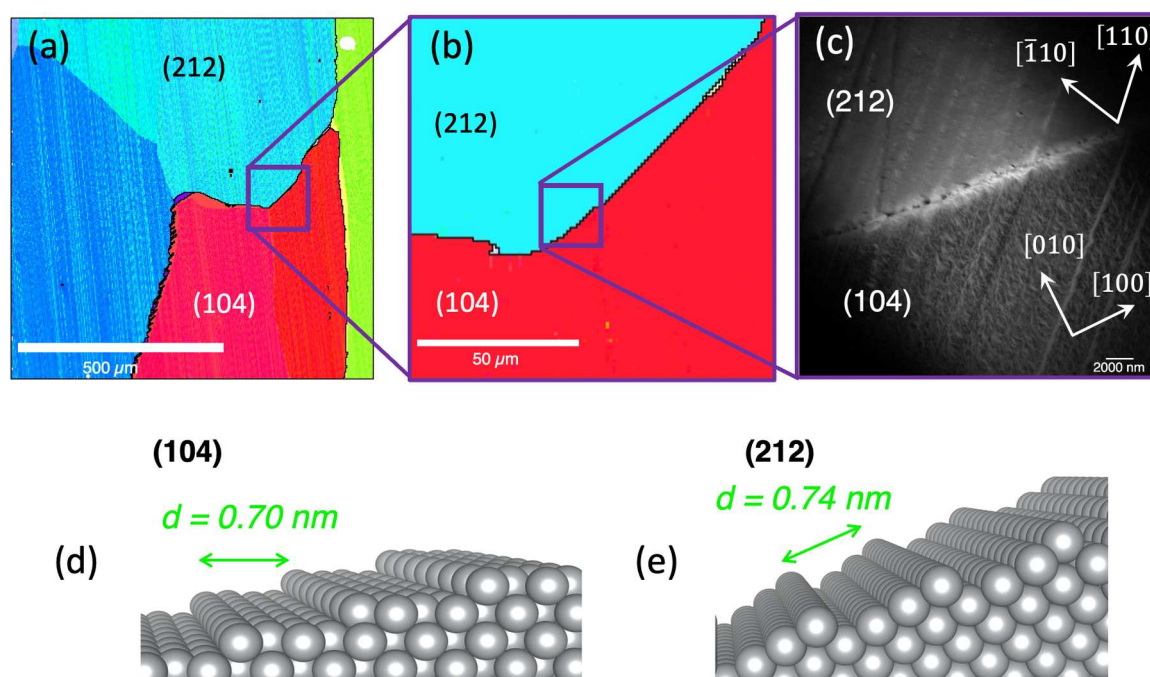
Fig. 1. (a) EBSD map of the Ni22Cr surface before oxidation; (b) the area of interest marked in (a). (c) XPEEM mode image taken in-situ of the region of interest before oxidation. The XPEEM experiment area was identified by using successively smaller magnification and feature matching of grain boundary and shape of adjacent grains to EBSD. (d) and (e): structure model of the respective alloy surface. The terrace width is marked.
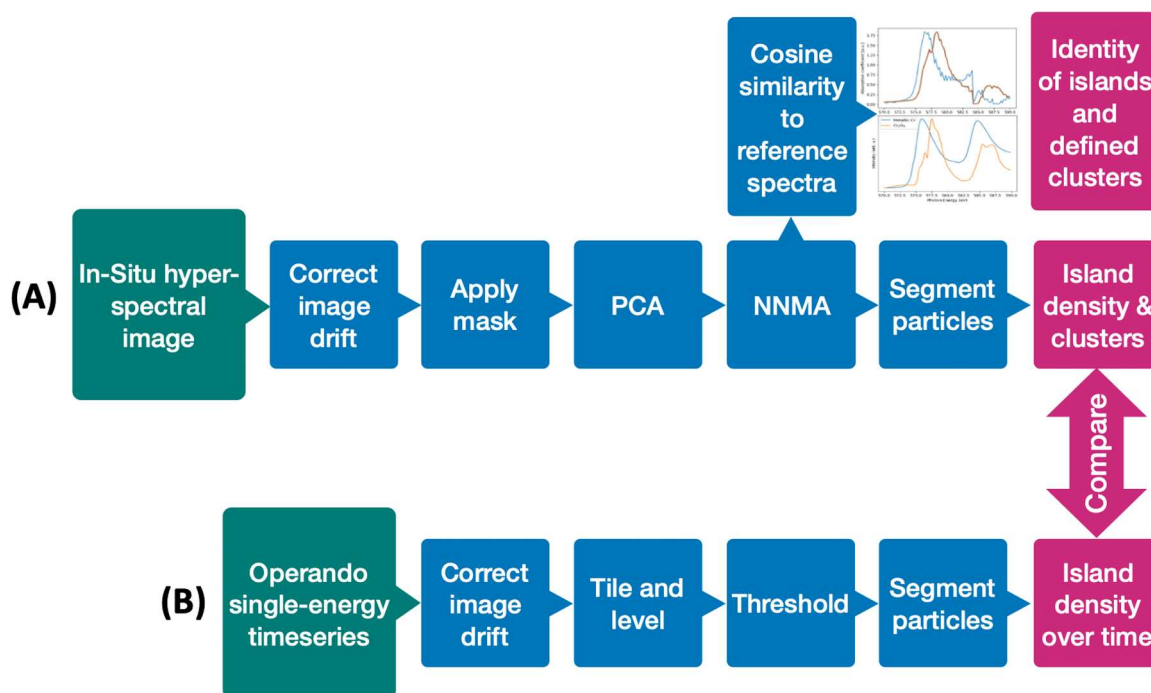
Fig. 2. Schematic representation of the workflow for XPEEM image analysis for (A) hyperspectral images and (B) timeseries images.

recorded for three time-windows using single-energy[47] μ-XAS. The photon energy was set to 577.5 eV at the Cr L_3-edge since it aligns with the Cr_2O_3 feature and a laboratory XPS study confirmed that only traces of NiO are detected under identical oxidation conditions. It is hence sufficient to monitor the Cr L_3-edge. The videos from the time series (Fig. 2.(a)) are available on Mendeley Data [49]. Fig. 2.(a) summarizes the analysis of the μ-XAS hyperspectral images. They were processed by correcting for image drift, normalizing of spectra to unit height, and masking noisy spectra regions at the image edges. The images were then analyzed using data-dimensionality reduction techniques, including PCA, NNMA, and cosine similarity in combination with a linear fit method using reference spectra. The large number of spectra within a hyperspectral image necessitates this approach.

Two complementary data dimensionality reduction techniques, PCA and NNMA, were used for the hyperspectral images (Fig. 2.(a)) to identify significant compounds (metal and oxide) and to access their spatial distribution. PCA decomposes the spectra into a set of orthogonal components that can be linearly combined to construct the original dataset through the relationship $D = SL^T$, where D is the original data, S is a matrix of scores, and L is the matrix of loadings (also referred to as principal components).[51] The dataset is a matrix with the shape ($n_{pixels} \times m_{variables}$) where $m_{variables}$ is the number of energy values in a spectrum. Each component is a row in the loading matrix with same dimensions as the XAS spectra ($m_{variables}$). These components are ranked in order of importance, and typically only a few components are needed to represent most of the variation in the data. A component is typically determined to be significant if it accounts for a significant amount of data variance, $> 5 \%$ for example. A score for each observation, the dot product between a spectra and a component, can be interpreted similarly to the concentration of that component at each pixel.[51] By reshaping the score for each pixel into an image, variation in space and concentration can be linked.[52] For a detailed explanation of PCA's application to large spectral datasets and hyperspectral images, see excellent explanations in Beattie et al. [51] and Lerotic et al. [52] respectively.

NNMA, unlike PCA, is an iterative method that constrains the components, so that they follow the rules of real spectra but this means they lose the constraints of orthogonality.[53] NNMA is also referred to as

non-negative matrix (NMF) factorization in literature,[54] and has been used to study hyperspectral XAS images.[55] What distinguishes NNMA used here from NMF often discussed in literature, is the addition of sparseness constraints which yields more interpretable components but slower convergence.[53] PCA is fast and mathematically meaningful, but the components are difficult to interpret compared to reference spectra. NNMA is relatively slow and requires prior knowledge of the number of significant components, but since it follows the same physical rules as real spectra it is easier to interpret with respect to chemical information. PCA was performed to determine the number of significant components and informed the choice of the predefined number of components in the NNMA calculation. PCA calculations were performed with python scripts and the Mantis package, [56] and for NNMA only the Mantis package was used. The results of PCA are discussed in the Supplementary Information S3.

A linear combination of reference spectra is commonly used for XAS analysis and has been used to determine the Cr oxidation state by assuming that the experimental spectra are the sum of metal and oxide contributions.[57,58] The large number of relatively noisy spectra limited the speed and convergence of linear combination fitting, so cosine similarity was used. Cosine similarity is a quantitative vector comparison metric between spectra that has been used for large XAS datasets[59] and provides unbiased similarity metric.[60] Cosine similarity is computed by the dot product of each pixel spectrum (N_i) to a reference spectrum (Ref_x) and dividing by the product of these vector's magnitude. This is shown below in Eq. (1).

$$Cosine\ Similarity = \frac{Ref_x \bullet N_i}{||Ref_x||\ ||N_i||} \tag{1}$$

Cosine similarity is more limited than linear combination fitting[60] but because it is computed using the dot product instead of iterative solving methods it is easy to compute for large datasets.[61] This is critically advantageous for hyperspectral images that contain large numbers of noisy spectra. Before analysis of the XPEEM timeseries (Fig. 2.A) and the hyperspectral images, several artifacts were corrected for. The individual frames in the XPEEM time series were aligned to correct for drift using ImageJ/Fiji.[62] Regions of the timeseries and hyperspectral images that were too bright or too dark to analyze

accurately were removed by masking parts of the center and the edges of the images. This affected XAS spectra in the central region of the image. This procedure is discussed in more detail in the Supplemental Information S1. The time-series data (Fig. 2.B) were affected intermittently by loss of focus, which can be seen in the videos [49] as a gradual loss of resolution for short periods followed by a sharp re-focus after manual correction, this is shown in the Supplemental Information S1. These unfocused images are excluded from the time-series analysis which leads to two time-gaps. The oxide island distributions from the time series after segmentation were compared to the oxide distribution measured in the hyperspectral images which include the complete chemical information. Python codes used for data preparation and analysis are available on Github (github.com/keithen-orson/XPEEM_NiCr) and discussed in the Supplemental Information.

To measure the oxide island density and size distribution in the timeseries datasets the images must be segmented, i.e. separated into island and background. However, segmentation solely based on a global intensity thresholding in the as-measured timeseries images is not accurate because of background intensity variations over time and space. [47] Therefore, the images were divided into 64×64 pixel tiles and these tiles were then plane leveled individually to account for varying background intensity - see "tile and level" step marked in Fig. 2.B. Islands could then be identified by setting a local threshold. The optimal threshold was determined to be the median+ 12.2 % of overall image intensity. This was determined by comparing different threshold conditions to annotated images using the accuracy metrics adapted rand error, precision, and recall. Quantification of segmentation accuracy is discussed in detail in the Supplemental Information S2.

3. Results

3.1. Observations from the XPS measurements

The results from the laboratory XPS experiment are summarized in Fig. 3 which includes the Cr $2p_{3/2}$ and Ni $2p_{3/2}$ core levels as a function of oxygen exposure. The exposure times match the ones for XPEEM hyperspectral images. The pre-oxidation measurement after annealing to 600 ℃ and flashing repeatedly to 700 ℃ confirms that native oxide is removed. The Cr $2p_{3/2}$ and Ni $2p_{3/2}$ core levels show the pristine alloy. The Ni $2p_{3/2}$ peak is positioned at 853.6 eV, and Cr $2p_{3/2}$ at 574.8 eV. [63] The changes in the Ni core level during oxidation are minute, and only a slight increase in intensity between 856 and 858 eV indicates a small oxide contribution. Even exposure to 120 L does not change the Ni $2p_{3/2}$ core level. In contrast, Cr oxidizes immediately and Cr_2O_3 is present in significant amounts even after 20 L of oxygen exposure. The spectral shape of the Cr $2p_{3/2}$ core level is consistent with Cr(0) and Cr_2O_3 and the fit is included in Fig. 3(b). [63,64] The oxide consists almost exclusively of Cr_2O_3 and the alloy surface becomes depleted in Cr: the fraction of Ni(0) in the alloy is 78 % before oxidation, 94 % Ni at 20 L of exposure and 97 % Ni after 65 L of exposure with Cr(0) as the balance to 100%. This is expected for oxidation at 500 °C where bulk diffusion is not sufficient to replenish the Cr used during oxide formation. Consequently, this leads to the sub-surface alloy composition within the information depth of XPS becomes Cr deficient.[65] The thickness of the chromia layer is estimated via the Strohmeier formula [66] using an inelastic mean free path of 2.1 nm for Cr_2O_3 and 1.6 nm for Cr.[67] The Cr_2O_3 equivalent thickness, assuming a uniform layer, is 1.5 nm, and 2.2 nm after 20 L and 65 L oxygen exposure, respectively. The near exclusive oxidation of Cr and presence of Cr_2O_3 supports the choice of the Cr L_3-edge in XAS for the XPEEM experiments.
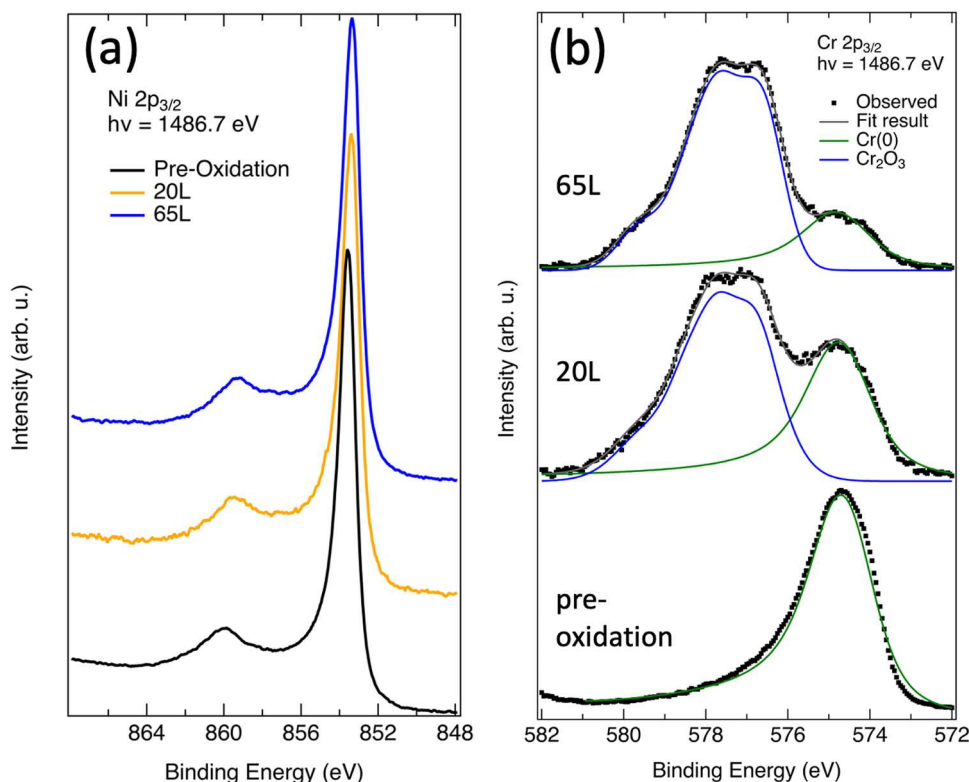
Fig. 3. XPS measurements of the oxidation process showing (a) Ni $2p_{3/2}$ and (b) Cr $2p_{3/2}$ core levels with fit including alloy and oxide peaks. For visualization purposes the spectra are normalized to unit height and a Shirley background is removed for the Cr 2p core level. The fit for the oxide component (blue) is the envelope of the multiplet.

3.2. Hyperspectral images

Fig. 4 shows the Cr and Ni L₃-edge spectra extracted from the hyperspectral images for the pristine alloy, 5 L, 20 L, and 65 L of exposure averaged over the entire image. Reference spectra for Cr(0) and Cr₂O₃ are included in Fig. 4(c). These were measured by exposing Ni-15at%Cr to $p(O_2)= 10^{-6}$ torr for 50 min which is the equivalent of 4200 L [Brookhaven National Laboratory, Beamline 23-ID-2, unpublished results]. This oxidation produced a thick oxide layer suitable for use as an experimental Cr₂O₃ L-edge XAS reference spectrum and the oxide film thickness exceeds the information depth of the measurement. No Cr(0) remains within the information depth in this measurement and the alloy surface can described as completely covered with an oxide layer. The Cr₂O₃ reference spectrum has no spectral weight at the Cr(0) edge position and the shift of the edge due to the oxidation state is readily apparent. The spectral shape, and peak positions agree with published measurements for Cr₂O₃.[68] The overall progression of the oxidation from Fig. 4(a) shows the increasing contribution from oxide spectral features to Cr L₃. The Cr L₃ edge shows very little change until an exposure of at least 20 L is reached, where a broadening at high energy side of the L₃ peak is observed. At 65 L, a second peak assigned to Cr₂O₃ appears at 577.5 eV.[68] The Ni L₃,₂-edge (Fig. 4(b)) remains unchanged in agreement with the XPS results, and the analysis therefore focusses on the components at the Cr L₃-edge.

Three principal components are sufficient to describe 98 % of the cumulative variance in the Cr L₃ hyperspectral images. No chemically distinct components aside from Ni(0) are identified from PCA analysis for Ni L₃. NNMA was performed on the Cr XAS images using three components weighted towards sparseness. The results of the NNMA analysis are summarized in Fig. 5. Fig. 5(a) summarizes the spectra and components. Components 2 and 3 capture the variation in the Cr L₃-edge, including the shift in edge position related to the change in oxidation state. Component 1 appears to represent the average of all spectra in the image, as has been observed by others for PCA and is not specific to the present analysis.[51] Component 2 has a peak at 576.0 eV and closely resembles the Cr(0) spectrum, and component 3 exhibits the characteristic double peak of the oxide spectrum between 577.0 and 578.0 eV. The jump in intensity at approximately 584 eV in both components is caused by an imaging artifact.

The score images of components 2 and 3 are shown in Fig. 5(b) and (c), respectively. Brightness in the score image is the dot product between the respective component and each pixel spectrum. In the score image in Fig. 5(b), brightness can be interpreted similarly to the concentration of component 3 (oxide). Fig. 5(b) shows islands that are spectrally distinct from the surrounding surface. In the component 2 score image, Fig. 5(c), brightness can be interpreted similarly to the concentration of component 2 (metal). Here the same islands appear dark with a higher brightness in the surrounding background, indicating more metallic contribution outside of the islands. A comparison between

NNMA score images and manual inspection of the measured spectra confirms the assignment for oxide and metal rich regions. The island density is higher in the (212) grain and lower in the (104) grain with a region close to the grain boundary that is only sparsely populated. A very weak signal might indicate a contamination with Sb but this interpretation has low confidence. The polishing scratches and grain boundary are more similar to component 3 Cr(0), as can be seen by their higher relative brightness in score image 5(c).

The analysis undertaken so far indicates two chemically distinct species, Cr(0) and Cr₂O₃, and cosine similarity was used to quantify the similarity of each pixel's L₃ spectrum (570–584 eV) to Cr(0) and Cr₂O₃, respectively. The pixel spectra are a mix of oxide and metal contributions– PCA and NNMA allowed us to identify the number and identity of the chemical species, and cosine similarity now offers quantitative information from the linear combination of reference spectra. Since only two spectra are used in the cosine analysis, a normalized cosine similarity is defined and given below in Eq. (2) where Ref$_x$ is the reference spectra, N_i is the spectrum at pixel *i*.

$$Normalized\ CS = \frac{\frac{Ref_x \bullet N_i}{||Ref_x||\ \ ||N_i||}}{\frac{Ref_{Cr2O3} \bullet N_i}{||Ref_{Cr2O3}||\ \ ||N_i||} + \frac{Ref_{Cr(0)} \bullet N_i}{||Ref_{Cr(0)}||\ \ ||N_i||}} = \frac{CS_X^i}{\sum CS^i} \tag{2}$$

The cosine similarity score images representing the quantitative contributions of Cr(0) and Cr₂O₃ to the Cr L-edge hyperspectral image at 65 L exposure are included in Fig. 6. Fig. 6(a) shows the construction of synthetic spectra with linear combination of Cr and Cr₂O₃ reference spectra covering the entire composition range from 100 % Cr to 100 % Cr₂O₃. Fig. 6(b) includes the function relating the cosine similarity values to the known fraction of metal and oxide in percent. The hyperspectral images in Fig. 6(c,d) show the quantitative information about oxide and alloy contributions to each individual pixel using cosine similarity to oxide and oxide fraction, respectively, derived from the function shown in Fig. 6(b).

The entire surface contains both oxide and metal contributions. The GB and one polishing mark have < 20 % oxide which is less than the surrounding area, while the distinct islands possess oxide contributions exceeding 60 %. The background pixels in Fig. 6(c,d) include mixtures of oxide and alloy. The relative contributions of oxide and alloy to all image pixels is summarized in Fig. 7. Fig. 7(a) shows a violin plot which visualizes the variation in oxide contribution derived from cosine similarity, and Fig. 7(b) includes representative spectra for island and background. It can be concluded that the surface is populated by distinct chromia islands. These islands are surrounded by a thinner oxidic layer which could be nanoscale islands, surface oxide (2D oxide), or O-adsorbate regions. The oxide islands also include some alloy contribution likely because their thickness is less than the information depth of the XAS. This agrees with the VB-PEEM and XPS observations, which support the presence of Cr-O phases and likely also nanoparticles of
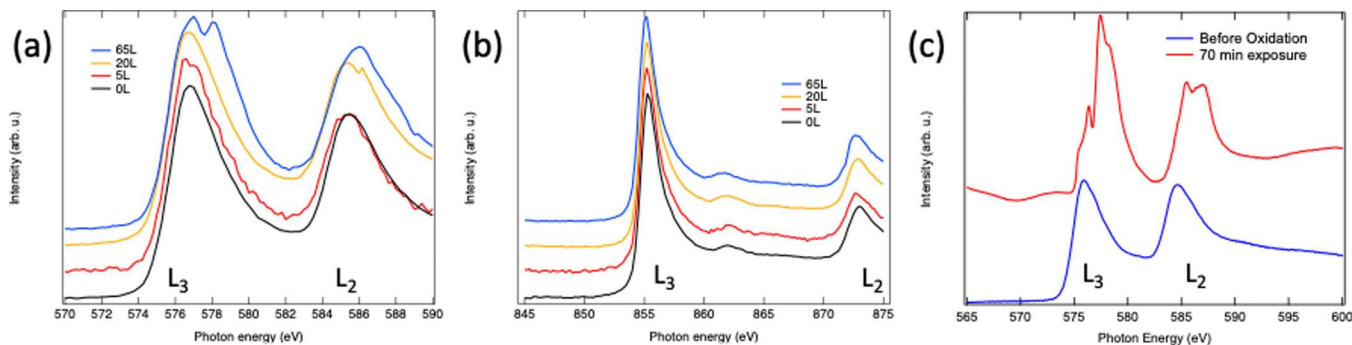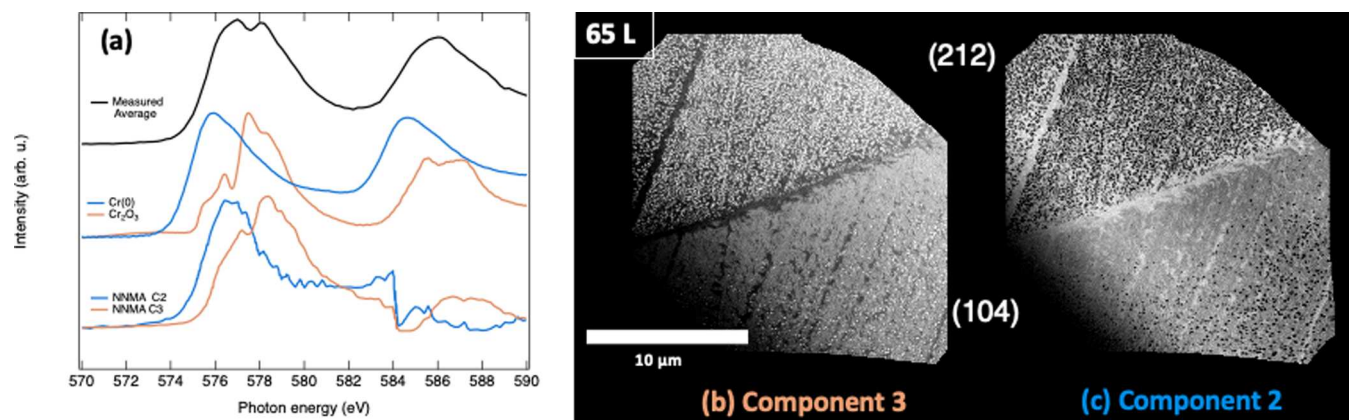

Fig. 4. XAS spectra averaged over the entire field of view in XPEEM for (a) the Cr L-edge and (b) the Ni L-edge throughout the oxidation. (c) an experimental reference for XAS spectra of metallic Cr and Cr₂O₃ produced by completely oxidizing Ni-15Cr for 70 min at $p(O_2) = 10^{-6}$ Torr at T = 500℃ to produce an experimental reference for Cr₂O₃.

Fig. 5. (a) Comparison of the XAS from hyperspectral images averaged over the entire image, the reference spectra for Cr and Cr_2O_3, and the NNMA derived components 2 and 3 for 65 L of exposure with greatest similarity to reference spectra (label Cr(0) and Cr_2O_3). Component 3 can be assigned to Cr_2O_3 and component 2 to Cr(0). (b) score image of component 3 where brightness is linked to Cr_2O_3 concentration (c) score image of component 2 where brightness is linked to Cr(0) concentration.
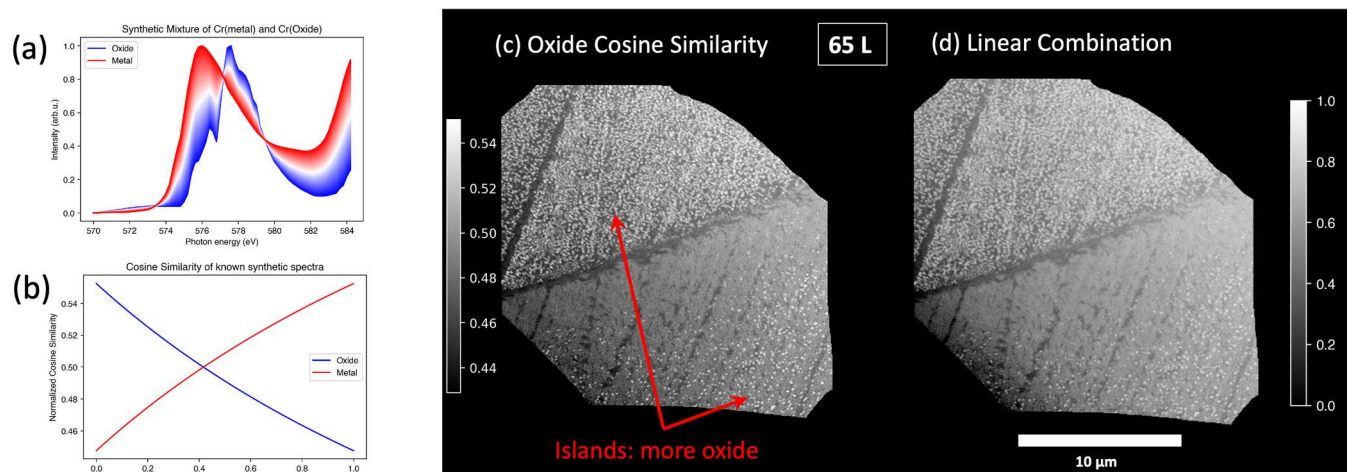
Fig. 6. (a) synthetic spectra including mixtures of oxide and metal spectra from zero to 100 %; (b) the cosine similarity calculated from the synthetic spectra covering the whole range from pure alloy to oxide. (c) Cosine similarity of the Cr L_3 edge hyperspectral image to Cr_2O_3. Image intensities are normalized to show contrast, and (d) the cosine similarity values translated to linear combinations of oxide and metal spectra.
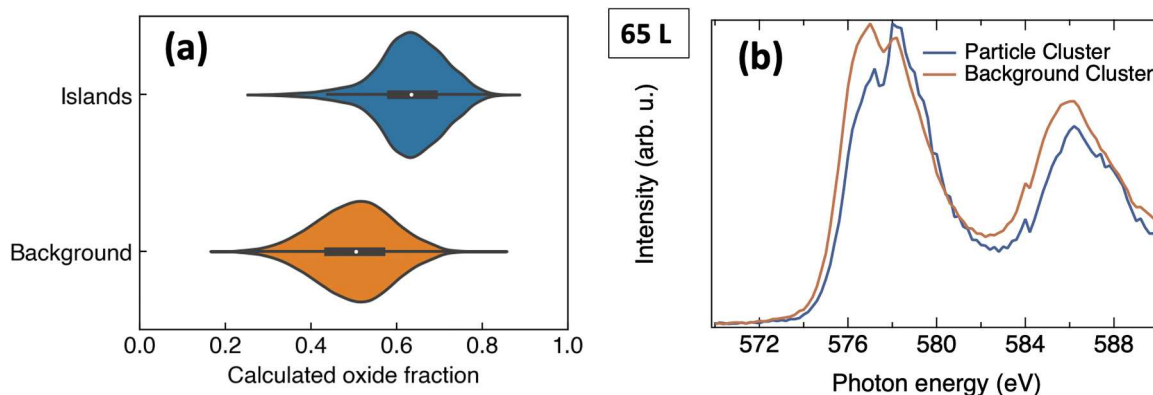
Fig. 7. Comparison of island and background contributions: (a) violin plot showing the cosine similarity for each pixel of the islands and background, and (b) the average Cr XAS L-edge spectra at 65 L of exposure for the islands (blue) and background (orange).

chromia early in the oxidation process and is commensurate with our earlier STM observations.[6–8]

The next step is thresholding and segmentation to quantify the oxide island density and size distributions throughout the time series. Island finding and segmentation using PCA, NNMA, and cosine similarity metrics produces very similar results, with a dice index of 0.98.[69] The details of this comparison are given in Supplemental Information S4. It is notable that the unsupervised methods, NNMA and PCA, deliver near

identical results to cosine similarity, where the choice of reference spectra is decided fully by the researcher.

Fig. 8 shows the result of segmentation of score image for NNMA component 3 from the Cr µ-XAS. The segmentation is done in ImageJ/FIJI after manual selection of a suitable global threshold value. Local thresholding and batch processing were not necessary for the score images since there are only a few images and score images are not affected by overall intensity variations. The evolution of particle densities and size distribution with time is shown in Fig. 9 as the result from the single energy timeseries data. Three pixels are used as the smallest area to be counted as an oxide island which is an area of about 50 nm^2 and island diameter of ~7 nm. On the (212) grain, the average island density is 5.73 islands/µm^2 with an average island size of 0.040 µm^2. The island distribution is quite uniform even adjacent to the grain boundary and only slightly perturbed in the vicinity of a few more prominent polishing scratches. The overall island coverage is 24 % and the average distance between islands is 0.27 ± 0.07 µm. The island distribution on the lower (104) grain is nonuniform with the lowest density of islands near the grain boundary. The average island density across is 1.94 islands/µm^2. About 5 µm from the grain boundary, where the island distribution is homogeneous, the island density has reached 5.76 islands/µm^2 which corresponds to 17 % coverage with an average island size of 0.029 µm^2.

3.3. Time-series and island evolution

Fig. 9 showcases three frames extracted from the operando oxidation timeseries [49] to illustrate the emergence of chromia islands. The background has some darker variations on a longer length-scale which cannot be tied to a specific chemical state in the XAS spectra. They are likely caused by local variation in secondary electron emission intensity and work function, possibly due to adsorbed oxygen or the presence of other pre-chromia oxidic contributions. VB-PEEM spectra are more surface sensitive and offer insight in the origin of this contrast and are discussed below. The time series is recorded at a single photon energy of 577.5 eV which aligns with the Cr$_2$O$_3$ feature in the Cr L$_3$ peaks, and allows us to track the evolution and growth rate of the oxide islands with a time resolution just below 10 s. The smallest islands included in the count occupy an area of 3 pixels. Some instances of de-focusing are observed across the entire image causing time gaps in the datasets: (i) around 37 L followed by manual re-focusing around 44 L, (ii) a few dips in the island count around 52 L and 55 L in both the upper and lower grain images. The final island densities from XAS hyperspectral images at 65 L agree well with extrapolated values from the time series which ends at 57.6 L.

The island density, size distribution, and median area are included in

Fig. 10. In Fig. 10(a) the island density as a function of time shows that islands emerge for the (212) grain at about 30 L of exposure and thus significantly earlier than for the (104) grain. This is followed by a steep increase in island density and a leveling off at about 50 L, and growth begins to dominates over nucleation. For the (104) surface, the islands become visible at about 45 L and the island density increases with a constant but shallower slope throughout the experiment. The overall density for the lower (104) grain includes the denuded region, so the overall density is expected to be lower. The median island size increases from 5.0×10^{-3} µm^2 (4.5×10^{-3} µm^2) to 7.5×10^{-3} µm^2 (6.5×10^{-3} µm^2) for (212) and (104), respectively. The increase in island size is reflected in the size distributions in Fig. 10(c,d) where distributions observed early and late in the oxidation experiment are compared. For both grains the distribution has a maximum at small island sizes and over time the abundance of larger island increases with a concomitant loss of smaller ones. The island evolution seen here is characteristic of the transition from nucleation to island growth, ripening and eventually coalescence.

3.4. Valence band spectra – VB-PEEM

VB hyperspectral images with 1024 × 1024 pixels for the alloy surface at 0, 20 and 65 L of oxygen exposure were collected in addition to the XAS hyperspectral images at the L-edge. The photon energy was 100 eV which corresponds to an electron mean free path of about 0.6 nm and is therefore highly surface sensitive. The energy range for the VB spectra is 5.0 eV and $\Delta E = 0.2$ eV. Fig. 11 (a-c) shows hyperspectral images for select binding energies chosen to maximize contrast for metallic or oxidic contributions, and Fig. 11(d) includes representative VB spectra of distinct regions in the hyperspectral images which are labeled according to brightness in correspondence with marked regions in (a-c). The VB spectra on the (104) grain follow the same general trends throughout the oxidation, but a small oxide contribution is visible in the denuded region already on the alloy prior to the oxidation experiment. The spectra are displayed with two x-axes: the kinetic energy, which is measured directly, and the binding energy, which is determined by positioning the Fermi energy (E$_F$) at the inflection point of the Fermi edge.

The alloy before oxidation on (212) shows an intense peak close to E$_F$ from the Ni-Cr d–band.[70–72] The binding energy of 0.2 eV chosen for the hyperspectral image slice in Fig. 11(a,b) is close to E$_F$ and the brightness in the image scales with the contribution from metallic states. The "large area average" spectrum and the VB spectra recorded for the "bright" regions after 20 L and 65 L exposure correspond to the highest metallic contributions within the images. The "grey" regions in Fig. 11 (a,b) have a lower density of states at E$_F$ and a shoulder centered at
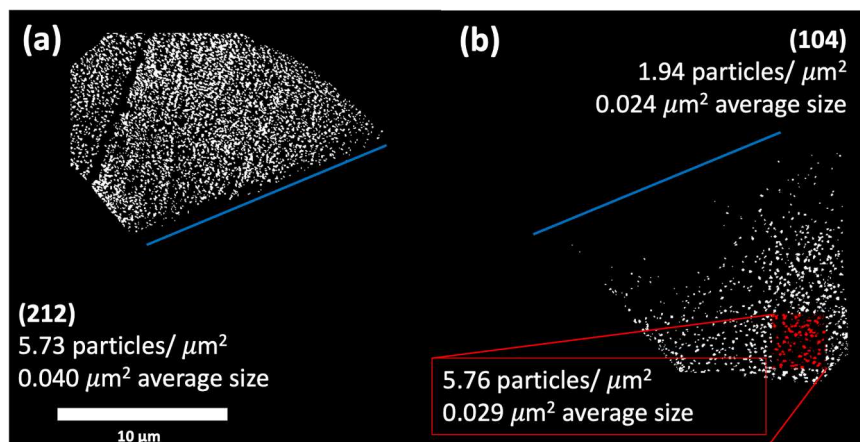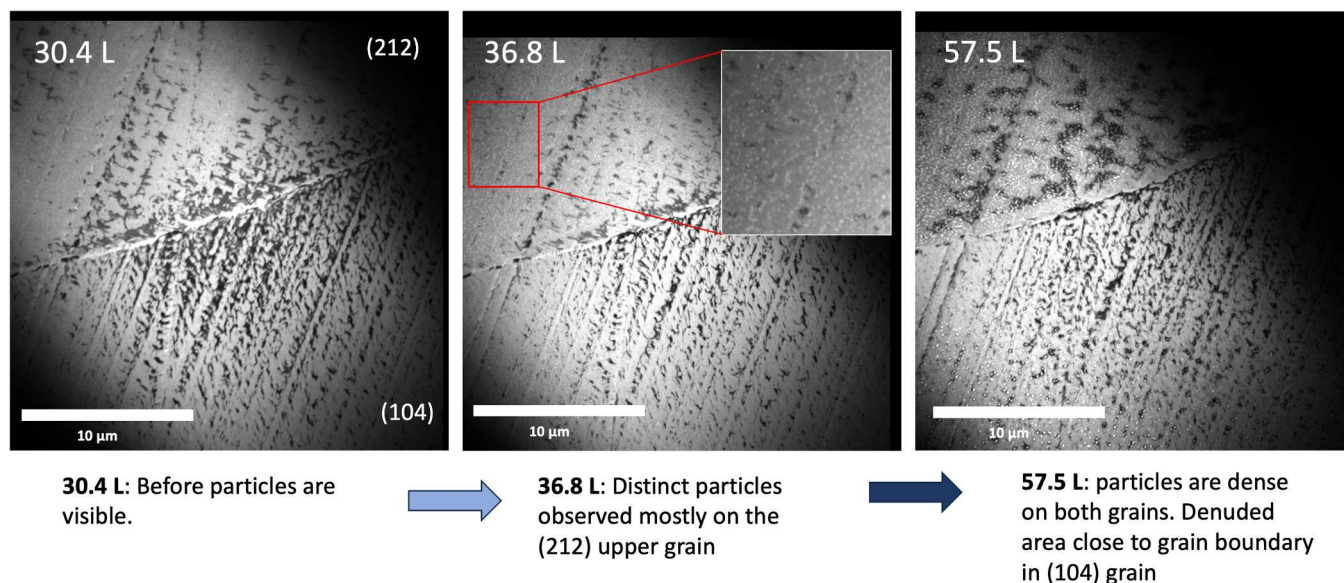

Fig. 8. Result of islands segmentation using a manual threshold of the NNMA score image from (a) the upper (212) grain (b) and the lower (104) grain. The grain boundary is marked in blue, and the denuded region on (104) is excluded in the count. The blue line indicates the grain boundary.

Fig. 9. Select frames from the single energy timeseries (video) showing the emergence and growth of the chromia islands. The series is recorded at a fixed photon energy of 577.5 eV, which coincides with the chromia signal. The complete videos are included in the Supplemental Material.
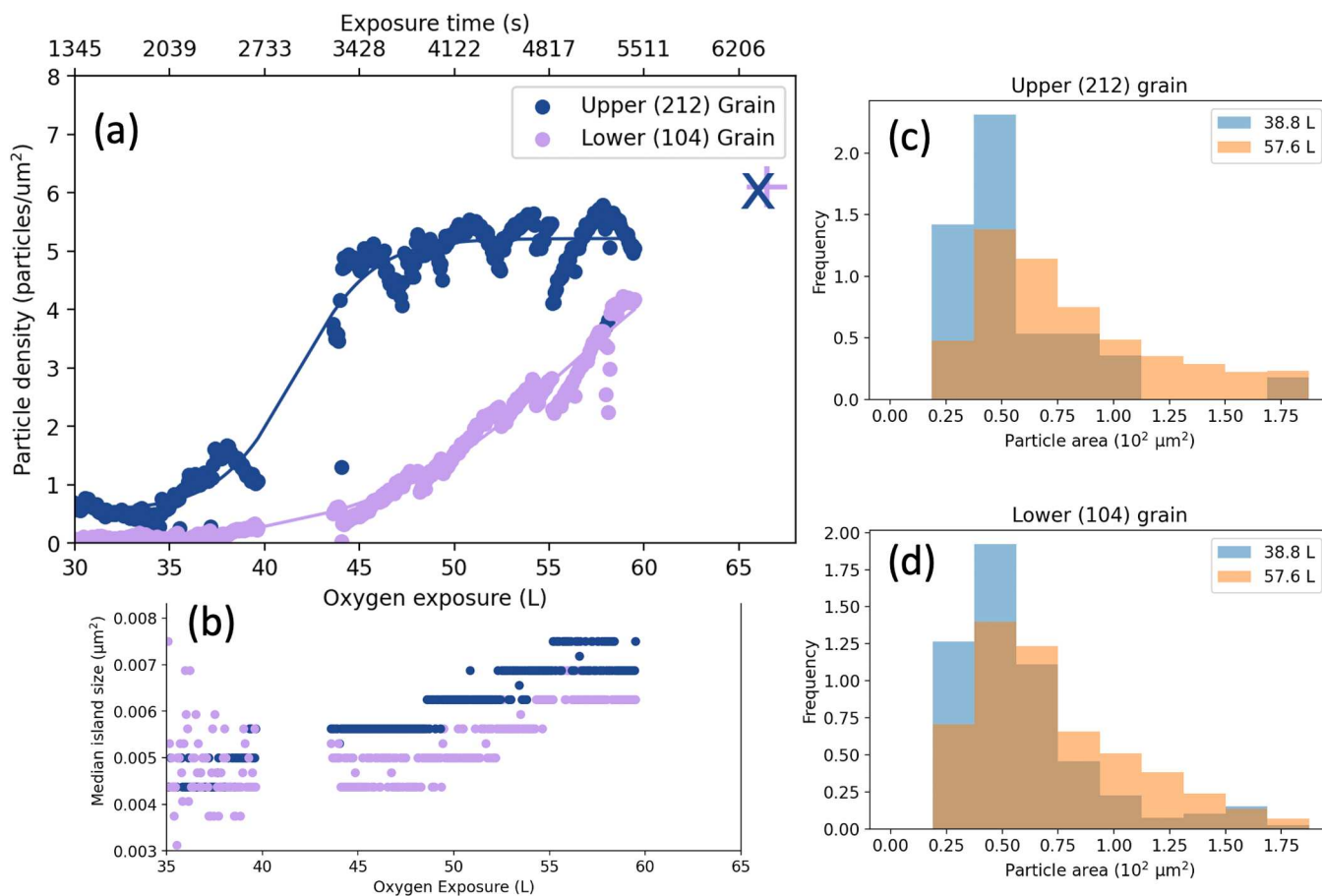
Fig. 10. (a) Time dependence of the island density determined by thresholding. Gaps in the graph correspond to de-focusing events. The "+" and "x" symbols represent the overall cluster density determined from NNMA cluster analysis for the XAS hyperspectral images.
(b) Median island size, and.
(c,d) island size distributions for both grains at exposure when oxide islands become first visible, and at the end of the video. The distributions are normalized to the island count.
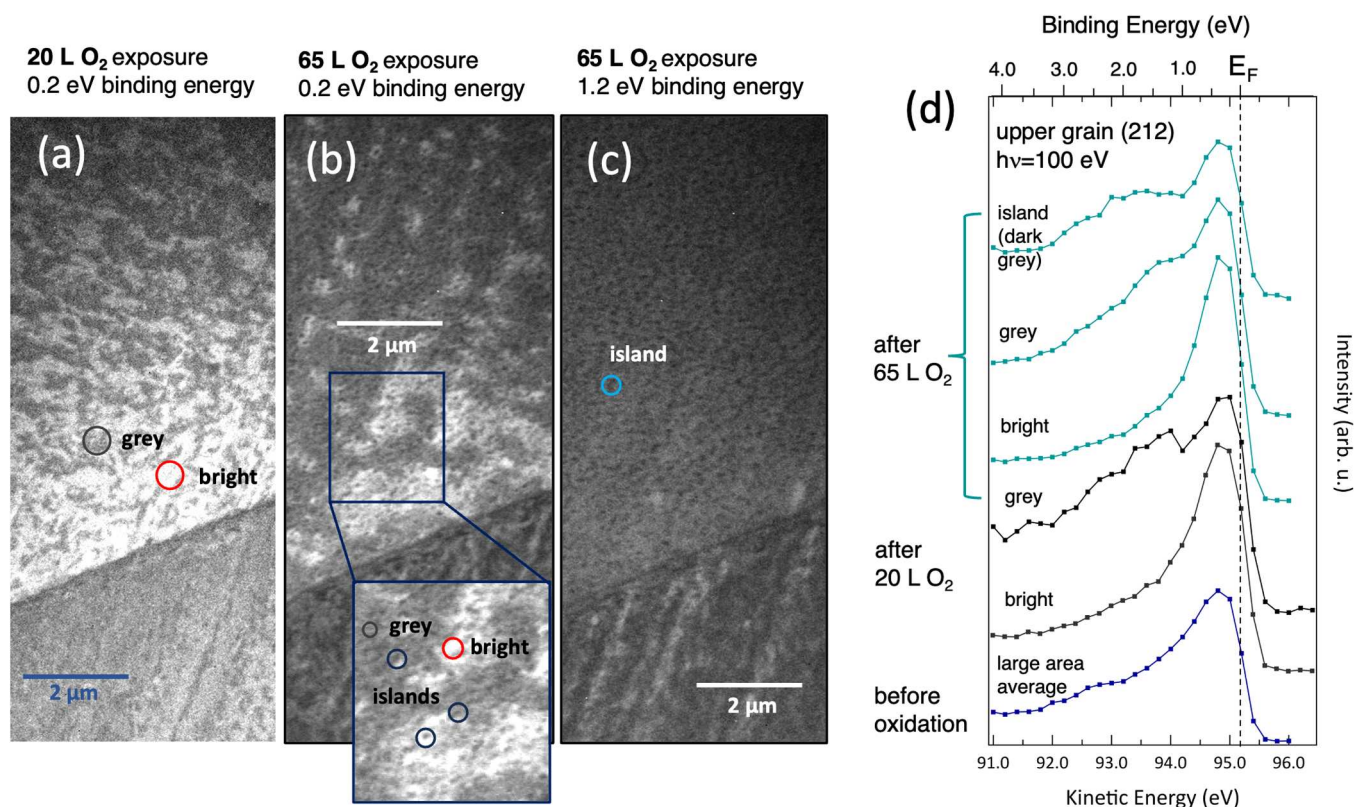
Fig. 11. Slices of hyperspectral valence band XPEEM image stacks for select energies. The slices are selected to maximize contrast for metallic or oxidic contributions. The grain boundary between (212) and (104) bisects the images. (a) image slice at 0.2 eV at the maximum density of states for the alloy measured after 20 L of exposure. (b) image slice at 0.2 eV after 65 L of exposure. Examples for bright, and grey regions are circled in (a) and (b). The inset shows in more detail the oxide islands which appear as the darkest and localized feature. Two islands are marked with a blue circle: one embedded in a bright region (metallic) and one embedded in a grey region (more oxidic). (c) image slice at 1.2 eV which selects for contrast in the oxidic contributions. (d) Representative valence bad spectra from distinct regions in the hyperspectral images.

~2.0 eV binding energy develops and is indicative of the onset of oxidation. The O 2p-states interact with the alloy 4 sp- and 3 d-bands and hybridization leads to the characteristic oxygen related peaks. The 3d hybridized band is located between 1.5 eV and 3.0 eV for Cr-oxides, and O 2p hybridized states would be seen at about 5.0 eV but are outside the energy window in this experiment. [73,74] [75] The spectral changes can be interpreted as regions of O-adsorption, surface oxides, or nanocrystalline oxidic particles. The oxidic regions are relatively large with ragged boundaries and cover a large percentage of the surface. Well-defined oxide islands are only visible at 65 L in Fig. 11(b,c) and appear as "dark grey" islands.[7,8] Their distribution correlates well with the XAS analysis. In the valence band spectra of the "islands" the alloy contributions are further diminished and oxidic states are prominent. Fig. 11(c) includes an image slice at 1.2 eV binding energy which maximizes contrast for the oxide islands appearing now as "dark grey". The slightly higher intensity of the background, labeled "grey" in Fig. 11 (d) is due to the larger contribution from the alloy which is only covered by a thin oxidic adsorbate layer.

The observed chemical heterogeneity across the surface can be explained by co-existence of a thin layer of oxidic species and chromia islands. The VB-XPEEM observations agree with the XAS analysis (see also Fig. 6 for cosine similarity results) and force us to rethink the mechanism of oxidation, and its consequence for the formation of a high-performing protective oxide layer. These observations lead us to conclude that the growth mode of chromia islands is, in essence, a mixed mode where layer and island growth occur during the early stages of oxidation. This is reminiscent of the Stranski-Krastanov growth mode, which has been observed in strained systems such as Si-Ge where a wetting layer is formed prior to nucleation of distinct islands. This

observation is in agreement with earlier STM from our group on early-stage Ni-Cr oxidation using (100) and (111) surfaces. STM has a higher spatial resolution than XPEEM but is not sensitive to the details of the island chemistry. STM and XPEEM can be seen as complementary methods but differ in the information they can provide. [7,14]

4. Discussion

The present study opens a detailed view of the initial oxidation reactions on Ni-22Cr alloy at the transition of an alloy surface to the formation of oxide islands. The use of XPEEM delivers simultaneously nanoscale chemical, spatial and temporal resolution which enabled us to follow the oxide formation in real time. The heterogeneity overserved in these oxides develop from compositional and microstructural variations in the surface. These are important factors in its long-term performance and can ultimately limit protectiveness. In this work the oxidation of two alloy grains is compared: (104) which is a 4(100)× (110) surface, and (212) which is a 4(111)× (111) structure. The nomenclature n(h k l)× (h k l) denotes the terrace with "n" as the number of atom rows followed by the crystallographic orientation of the step. By coincidence, the two grain surfaces have terraces with very similar widths but different orientation. The grains are separated by a grain boundary (GB) and a few polishing grooves are visible. However, only one larger polishing groove on the left-hand side of the (212) grain appears to significantly influence the development of the oxide layer.

The GB bisecting the images stays predominantly metallic during oxidation. This behavior seemingly contradicts a common assumption of preferential oxidation caused by a high density of active sites. The relatively low p(O$_2$) throttles the reaction kinetics at the alloy surface

and enables us to observe the oxidation process with XPEEM. It is suggested that slow supply of oxygen combined with rapid metal atom diffusion along the GBs leads to more unreacted metal where the GB intersects with the surface, compared to grain surface which is highly depleted in metallic Cr according to the XPS results. Experimental data for bulk diffusion of Cr in Ni alloys can be found in Gheno et al. for temperatures between 542 °C and 843 °C. [76] They measure the diffusion coefficient at 542°C to be 9.3×10^{-19} cm^2/s. Our oxidation duration is 8800 s, which gives a characteristic diffusion length $(D*t)^{1/2}$ of 0.9 nm at 542 °C. Using their constants for the Arrhenius relationship for Cr bulk diffusion in Ni gives a diffusion coefficient of 1.0×10^{-19} cm^2/s and a characteristic diffusion length of 0.3 nm over the duration of our experiment. For the grain boundary diffusion of Cr in NiCr alloys Simonnin [77] shows that at high temperatures (1300K-1600K) grain boundary diffusivity can be four orders of magnitude faster than in the bulk and has an activation energy of 0.81 eV compared to the experimental value of 2.9 eV in the bulk.[8] The question of surface diffusion is much more difficult to address. Experimental data for surface diffusion coefficients for Cr on Ni is not available to the best of our knowledge. The activation energy of adatom Ni surface diffusion on Ni ranges from 0.2 eV to 0.4 eV, [10] which is a typical range for surface diffusion coefficients although step activation barriers can dominate in real systems.[11] The relative magnitude of diffusivity therefore could indeed allow for replenishing of Cr at the GB.

In addition, a significant part of the (104) lower grain in the vicinity of the GB is nearly denuded of oxide islands but shows in the VB-XPEEM spectra slightly more oxide remnants than other parts of the surface. The origin of this denuded region remains an open question and might be due to the contamination with trace elements which impede nucleation. Therefore, the discussion of oxidation process for (104) focusses on the regions where a homogeneous oxide island density is observed (see Fig. 8).

The oxidation reaction begins with the adsorption of oxygen, and formation of surface oxides, sub-oxides or nanocrystalline oxides as chromia island precursor. The initial oxidation step is seen clearly with VB-PEEM hyperspectral images where the attenuation of the metal signal at E_F is accompanied with an increase in oxidic contributions. For exposures < 30 L, the intermediate reaction products will contribute to the image background with contrast variations on a longer length scale. This can be seen in Figs. 5 and 9 and is supported by the VB-PEEM and XPS analysis. It is proposed that oxidic features such as adsorbates, nanoparticles, surface oxides (2D oxides), and sub-stoichiometric oxide particles are already present at lower exposures and continue to co-exist with the chromia islands.[6,9,14] The growth mode for chromia cannot be described as a well-defined island growth or layer-by-layer growth but is more akin to a Stranski-Krastanov[25] type growth where a wetting layer coexists with islands. This model is not intended to imply here a role of epitaxy or strain that is generally associated with Stranski-Krastanov type growth modes but focuses on the combined layer and island formation. The co-existence of the layers and chromia islands is the origin of a significant heterogeneity observed at the surface. This can influence the continued growth of the oxide, the diffusion of reactants and the Ehrlich-Schwoebel barrier, as the oxide evolves towards the Mott-Cabrera and Wagner regimes.

The increase in island density for (212) follows a logistic function, agrees with the form of the Johnson-Mehl-Avrami (JMA) model for nucleation[78] while the coverage range for (104) is too limited to conclude the functional form. However, despite a reasonable functional agreement the utility of JMA is limited here by the coexistence of precursor or intermediate oxidic configurations. In addition, the condition of constant reactant fluence for JMA is violated for Cr whose supply is controlled by the transport through the bulk alloy. So while the JMA model broadly fits the time-dependence it may not be appropriate for this system [79,80]. The earlier leveling off in the island density for (212) was initially thought to be caused by reduced Cr supply from the alloy although the nucleation rate of oxide islands is not impeded on

(104), and the existing islands on (212) continue to grow as seen in the island distributions (Fig. 10). These competing arguments might be reconciled if the Cr supply is sufficient to overcome the activation barrier for nucleation on (104) but not on (212). [17]

It can be argued that the variations in the oxide evolution and specifically in the evolution of chromia islands, is caused by variation in the crystallographic orientation. Prior work by Blades et al.[6,7] reported significant variations in oxidation for Ni-Cr single crystal (100) and (111) surface, and dependence of passive layer formation on the grain orientation is also seen in aqueous corrosion.[19,27] Hence the presence of (100) and (111) terraces in the two surfaces studied might indeed lead to the observed variation in chromia island evolution. A larger set of surface orientations is needed to fully capture the role of crystallographic orientation. In summary, the transformation of the alloy begins with the formation of a complex layer of chromia precursors with an abundance of oxidic Cr-O bonds leading to a oxide growth mode reminiscent of Stranski-Krastanov.

The results presented here make a strong argument for using unsupervised machine learning techniques for the inspection and analysis of hyperspectral, and time series data. The size and complexity of the datasets requires augmenting well-established methods in XAS analysis with PCA, NNMA, and related methods. NNMA and PCA can also identify sources in spectral variation that come from experimental artifacts and appear as an additional component, which can help prevent over-interpretation of data. Identifying the components builds naturally into quantifying relative concentrations of Cr and Cr$_2$O$_3$ using cosine similarity to reference spectra for Cr and Cr$_2$O$_3$. Additional challenges to the translation of qualitative information to quantitative information arise from the experimental factors such as uneven illumination of the field of view, and drift to loss-of-focus events. The experimental variability limits thresholding and segmentation without corrections. PCA, NNMA, and cosine similarity work in concert and lead to a reasonable segmentation process to understand island development. The use of several methods with different strengths such as PCA and NNMA proved to be critical and allowed us to test the outcomes of each procedure. In addition, a laboratory based XPS experiment offered an important independent check on the oxide composition.

Overall, the analysis of hyperspectral and time series datasets can be performed successfully using the following workflow (see Fig. 2): (1) Correct for drift, and variations in illumination. (2) Perform PCA to identify how many different components are present. (3) Perform NNMA to gain insight into what compounds are present based on physically meaningful reference spectra, and isolate components which might be introduced by experimental artefacts. (4) Use a quantitative metric, like cosine similarity, to determine relative concentrations of those species across the image in hyperspectral images, and (5) apply thresholding and segmentation algorithms to hyperspectral and time series datasets. Comparison of segmentation for both data types at set experimental condition serves as a check on the overall process.

5. Conclusions

The oxidation of Ni-22Cr at 500°C is studied using a combination of in-situ and operando techniques. The dominant oxide is Cr$_2$O$_3$, which accumulates in prominent islands embedded in a layer of adsorbates, and other oxidic or sub-stoichiometric intermediates. The results described here show that the oxide growth mode is akin to a Stranski-Krastanov, a combined layer and island growth. Altered oxide morphology at the grain boundary and (some) polishing grooves, and a significant difference in chromia formation and growth as a function of crystallographic orientation contribute to the heterogeneity of the surface. The role of trace contaminants emanating from the grain boundary remains an open question and must be addressed in future work. XPEEM and related method offers unique insight in dynamics of oxidation. The complexity of the process can only be fully captured through an implementation of several analytical tools from statistical and machine

learning techniques. Segmentation and thresholding are required to capture the quantitative information on oxide evolution from the operando time series, which proved both challenging and informative. In conclusion, XPEEM and related techniques provide a unique window in the processes of oxidation and passive layer heterogeneity at alloy surfaces.

CRediT authorship contribution statement

Petra Reinke: Writing – review & editing, Writing – original draft, Supervision, Project administration, Conceptualization. **Alexei Zakharov:** Investigation. **Yuran Niu:** Investigation. **Zachary Harris:** Data curation. **Anna Costine:** Investigation, Data curation. **Will Blades:** Data curation, Conceptualization. **Keithen G. Orson:** Writing – review & editing, Writing – original draft, Methodology, Investigation.

Declaration of Competing Interest

The authors declare that they have no known competing financial interests or personal relationships that could have appeared to influence the work reported in this paper.

Author contributions

W.H.B, A.C., P.R., Y.N. and A.Z performed the experiments. K.O. lead the data analysis, developed the image and data analysis tools and performed the XPS experiments. K.O. and P.R. lead the writing of the manuscript. The manuscript was read, discussed, and approved for submission by all authors. P.R conceived the study and acquired funding.

Appendix A. Supporting information

Supplementary data associated with this article can be found in the online version at doi:10.1016/j.jallcom.2024.178054.

Data availability

Data will be made available on request.

References

[1] G.C. Wood, B. Chattopadhyay, Transient oxidation of Ni-base alloys, Corros. Sci. 10 (1970) 471–480, https://doi.org/10.1016/S0010-938X(70)80032-4.

[2] B. Chattopadhyay, G.C. Wood, The transient oxidation of alloys, Oxid. Met. 2 (1970) 373–399, https://doi.org/10.1007/BF00604477.

[3] X.X. Yu, A. Gulec, C.M. Andolina, E.J. Zeitchick, K. Gusieva, J.C. Yang, J.R. Scully, J.H. Perepezko, L.D. Marks, In situ observations of early stage oxidation of Ni-Cr and Ni-Cr-Mo alloys, Corrosion 74 (2018) 939–946, https://doi.org/10.5006/2807.

[4] R.A. Rapp, Kinetics, microstructures and mechanism of internal oxidation - its effect and prevention in high temperature alloy oxidation, Corrosion 21 (1965) 382–401, https://doi.org/10.5006/0010-9312.21.12.382.

[5] L. Luo, L. Zou, D.K. Schreiber, D.R. Baer, S.M. Bruemmer, G. Zhou, C.M. Wang, In-situ transmission electron microscopy study of surface oxidation for Ni-10Cr and Ni-20Cr alloys, Scr. Mater. 114 (2016) 129–132, https://doi.org/10.1016/j.scriptamat.2015.11.031.

[6] W.H. Blades, P. Reinke, Early-stage evolution of nanoscale oxides on Ni(111) and Ni-Cr(111) surfaces, Corros. Sci. 209 (2022) 110755, https://doi.org/10.1016/j.corsci.2022.110755.

[7] W.H. Blades, P. Reinke, From alloy to oxide: capturing the early stages of oxidation on Ni-Cr(100) alloys, ACS Appl. Mater. Interfaces 10 (2018) 43219–43229, https://doi.org/10.1021/acsami.8b15210.

[8] W.H. Blades, M.R. Barone, P. Reinke, Initial atomic-scale oxidation pathways on a Ni–15Cr(100) alloy surface, Npj Mater. Degrad. 5 (2021), https://doi.org/10.1038/s41529-021-00164-7.

[9] L. Luo, L. Zou, D.K. Schreiber, M.J. Olszta, D.R. Baer, S.M. Bruemmer, G. Zhou, C. M. Wang, In situ atomic scale visualization of surface kinetics driven dynamics of oxide growth on a Ni-Cr surface, Chem. Commun. 52 (2016) 3300–3303, https://doi.org/10.1039/c5cc09165a.

[10] C. Volders, G. Ramalingam, V. Angelici Avincola, I. Waluyo, A. Hunt, P. Reinke, Oxidation of NiCr and NiCrMo alloys at low temperatures, Corrosion 79 (2023) 1287–1296, https://doi.org/10.5006/4400.

[11] C. Volders, V.A. Angelici, I. Waluyo, A. Hunt, L. Árnadóttir, P. Reinke, Unraveling the role of tungsten as a minor alloying element in the oxidation NiCr alloys, Npj Mater. Degrad. 6 (2022), https://doi.org/10.1038/s41529-022-00265-x.

[12] L. Luo, L. Zou, D.K. Schreiber, D.R. Baer, S.M. Bruemmer, G. Zhou, C.M. Wang, In-situ transmission electron microscopy study of surface oxidation for Ni-10Cr and Ni-20Cr alloys, Scr. Mater. 114 (2016) 129–132, https://doi.org/10.1016/j.scriptamat.2015.11.031.

[13] X. Wang, J.A. Szpunar, Effects of grain sizes on the oxidation behavior of Ni-based alloy 230 and N, J. Alloy. Compd. 752 (2018) 40–52, https://doi.org/10.1016/j.jallcom.2018.04.173.

[14] W.H. Blades, M.R. Barone, P. Reinke, Initial atomic-scale oxidation pathways on a Ni–15Cr(100) alloy surface, Npj Mater. Degrad. 5 (2021), https://doi.org/10.1038/s41529-021-00164-7.

[15] N.S. McIntyre, T.C. Chan, C. Chen, Characterization of oxide structures formed on nickel-chromium alloy during low pressure oxidation at 500-600°C, Oxid. Met. 33 (1990) 457–479, https://doi.org/10.1007/BF00666809.

[16] T. Gheno, F. Jomard, C. Desgranges, L. Martinelli, Tracer diffusion of Cr in Ni and Ni-22Cr studied by SIMS, Mater. (Oxf.) 3 (2018) 145–152, https://doi.org/10.1016/j.mtla.2018.08.004.

[17] A. Larsson, S. Gericke, A. Grespi, V. Koller, J. Eidhagen, X. Yue, E. Frampton, S. Appelfeller, A. Generalov, A. Preobrajenski, J. Pan, H. Over, E. Lundgren, Dynamics of early-stage oxide formation on a Ni-Cr-Mo alloy, Npj Mater. Degrad. 8 (2024) 39, https://doi.org/10.1038/s41529-024-00463-9.

[18] Y. Xie, D.M. Artymowicz, P.P. Lopes, A. Aiello, D. Wang, J.L. Hart, E. Anber, M. L. Taheri, H. Zhuang, R.C. Newman, K. Sieradzki, A percolation theory for designing corrosion-resistant alloys, Nat. Mater. 20 (2021) 789–793, https://doi.org/10.1038/s41563-021-00920-9.

[19] K. Gusieva, K.L. Cwalina, W.H. Blades, G. Ramalingam, J.H. Perepezko, P. Reinke, J.R. Scully, Repassivation behavior of individual grain facets on dilute Ni-Cr and Ni-Cr-Mo alloys in acidified chloride solution, J. Phys. Chem. C. 122 (2018) 19499–19513, https://doi.org/10.1021/acs.jpcc.8b04306.

[20] K. Lutton, W.H. Blades, J.R. Scully, P. Reinke, Influence of chloride on nanoscale electrochemical passivation processes, J. Phys. Chem. C 124 (2020) 9289–9304, https://doi.org/10.1021/acs.jpcc.9b12050.

[21] D. Young, High temperature oxidation and corrosion of metals, Second, Elsevier, Amsterdam, 2016.

[22] T.D. Reynolds, D.M. Collins, N.K. Soor, S.R. Street, N. Warnken, P.M. Mignanelli, M.C. Hardy, H.E. Evans, M.P. Taylor, Identifying heating rate dependent oxidation reactions on a nickel-based superalloy using synchrotron diffraction, Acta Mater. 181 (2019) 570–583, https://doi.org/10.1016/j.actamat.2019.10.019.

[23] W.H. Blades, E.J. Opila, K. Sieradzki, Mechanisms of exclusive scale formation in the high temperature oxidation of alloys, J. Electrochem Soc. 169 (2022) 061501, https://doi.org/10.1149/1945-7111/ac751f.

[24] J. Tersoff, A.W. Denier Van Der Gon, R.M. Tromp, Critical island size for layer-by-layer growth, Phys. Rev. Lett. 72 (1994).

[25] A. Baskaran, P. Smereka, Mechanisms of Stranski-Krastanov growth, J. Appl. Phys. 111 (2012), https://doi.org/10.1063/1.3679068.

[26] A. Atkinson, Transport processes during the growth of oxide films at elevated temperature, Rev. Mod. Phys. 57 (1985) 437–470, https://doi.org/10.1103/RevModPhys.57.437.

[27] J.C. Rao, X.X. Zhang, B. Qin, K.K. Fung, TEM study of the structural dependence of the epitaxial passive oxide films on crystal facets in polyhedral nanoparticles of chromium, Ultramicroscopy 98 (2004) 231–238, https://doi.org/10.1016/j.ultramic.2003.08.016.

[28] V. Maurice, W.P. Yang, P. Marcus, XPS and STM study of passive films formed on Fe-22Cr(110) single-crystal surfaces, J. Electrochem. Soc. 143 (1996) 1182.

[29] B. Zhang, J. Wang, B. Wu, X.W. Guo, Y.J. Wang, D. Chen, Y.C. Zhang, K. Du, E. E. Oguzie, X.L. Ma, Unmasking chloride attack on the passive film of metals, Nat. Commun. 9 (2018) 1–9, https://doi.org/10.1038/s41467-018-04942-x.

[30] P.H. Holloway, J.B. Hudson, Kinetics of the reaction of oxygen with clean nickel single crystal surfaces, Surf. Sci. 43 (1974) 123–140, https://doi.org/10.1016/0039-6028(74)90223-4.

[31] E. Kopatzki, R.J. Behm, Step faceting: origin of the temperature dependent induction period in Ni(100) oxidation, Phys. Rev. Lett. 74 (1995) 1399–1402, https://doi.org/10.1103/PhysRevLett.74.1399.

[32] E. Kopatzki, R.J. Behm, STM imaging and local order of oxygen adlayers on Ni (100), Surf. Sci. 245 (1991) 255–262, https://doi.org/10.1016/0039-6028(91)90028-Q.

[33] J.T. Stuckless, C.E. Wartnaby, N. Al-Sarraf, St.J.B. Dixon-Warren, M. Kovar, D. A. King, Oxygen chemisorption and oxide film growth on Ni{100}, {110}, and {111}: Sticking probabilities and microcalorimetric adsorption heats, J. Chem. Phys. 106 (1997) 2012–2030, https://doi.org/10.1063/1.473308.

[34] L.H. Sprowl, B.M. Adam, J.D. Tucker, L. Árnadóttir, First-principles study of the products of CO2 dissociation on nickel-based alloys: Trends in energetics with alloying element, Surf. Sci. 677 (2018) 219–231, https://doi.org/10.1016/j.susc.2018.06.011.

[35] G.T. Tyuliev, K.L. Kostov, XPS/HREELS study of NiO films grown on Ni(111), Phys. Rev. B 60 (1999) 2900–2907.

[36] V. Maurice, S. Cadot, P. Marcus, XPS, LEED and STM study of thin oxide films formed on Cr(110), Surf. Sci. 458 (2000) 195–215, https://doi.org/10.1016/S0039-6028(00)00439-8.

[37] L. Luo, M. Su, P. Yan, L. Zou, D.K. Schreiber, D.R. Baer, Z. Zhu, G. Zhou, Y. Wang, S.M. Bruemmer, Z. Xu, C. Wang, Atomic origins of water-vapour-promoted alloy oxidation, Nat. Mater. 17 (2018) 514–518, https://doi.org/10.1038/s41563-018-0078-5.

[38] L. Zhu, A. Al-Sakeeri, F. Lenrick, O. Darselius Berg, P. Sjödin, A.A. Zakharov, A. Knutsson, A. Mikkelsen, Surface chemistry and diffusion of trace and alloying elements during in vacuum thermal deoxidation of stainless steel, Surf. Interface Anal. 54 (2022) 99–108, https://doi.org/10.1002/sia.7024.

[39] J.I. Flege, A. Meyer, J. Falta, E.E. Krasovskii, Self-limited oxide formation in Ni (111) oxidation, Phys. Rev. B 84 (2011) 115441, https://doi.org/10.1103/PhysRevB.84.115441.

[40] J. Stringer, B.A. Wilcox, R.I. Jaffee, The high-temperature oxidation of nickel-20 wt % chromium alloys containing dispersed oxide phases, Oxid. Met. 5 (1972) 11–47, https://doi.org/10.1007/BF00614617.

[41] A. Stierle, H. Zabel, Oxidation induced roughening during Cr2O3(0001) growth on Cr(110), Surf. Sci. 385 (1997) 167–177, https://doi.org/10.1016/S0039-6028(97)00257-4.

[42] L. Ma, F. Wiame, V. Maurice, P. Marcus, Origin of nanoscale heterogeneity in the surface oxide film protecting stainless steel against corrosion, Npj Mater. Degrad. 3 (2019) 29, https://doi.org/10.1038/s41529-019-0091-4.

[43] E. Bauer, Photoelectron microscopy, J. Phys.: Condens. Matter 13 (2001) 11391–11404, https://doi.org/10.1088/0953-8984/13/49/316.

[44] N. Barrett, O. Renault, H. Lemaître, P. Bonnaillie, F. Barcelo, F. Miserque, M. Wang, C. Corbel, Microscopic work function anisotropy and surface chemistry of 316L stainless steel using photoelectron emission microscopy, J. Electron Spectrosc. Relat. Phenom. 195 (2014) 117–124, https://doi.org/10.1016/j.elspec.2014.05.015.

[45] G.P.P. Halada, J.R. Trelewicz, D.J. Sprouster, H. Yan, Y. Chu, E. Dooryhee, J. Sadowski, E. Coats, G.P. Manogharan, Use of Multi-Modal Synchrotron Analytical Techniques Combined with Electrochemical Analysis to Understand Anomalous Localized and General Corrosion Behavior of Additively Manufactured 316L Stainless Steel, 553, ECS Meet. Abstr. MA2021-02 (2021) 553, https://doi.org/10.1149/MA2021-029553mtgabs.

[46] T.H. Kang, K. Ihm, C.C. Hwang, J. Jeon, K.J. Kim, J.Y. Kim, M.K. Lee, H.J. Shin, B. Kim, S. Chung, C.Y. Park, Direct image observation of the initial forming of passive thin film on stainless steel surface by PEEM. in: Appl Surf Sci, Elsevier, 2003, pp. 630–635, https://doi.org/10.1016/S0169-4332(03)00137-5.

[47] Y. Niu, N. Vinogradov, A. Preobrajenski, C. Struzzi, B. Sarpi, L. Zhu, E. Golias, A. Zakharov, MAXPEEM: a spectromicroscopy beamline at MAX IV laboratory, J. Synchrotron Radiat. 30 (2023) 468–478, https://doi.org/10.1107/S160057752300019X.

[48] A.A. Zakharov, A. Mikkelsen, J.N. Andersen, Recent advances in imaging of properties and growth of low dimensional structures for photonics and electronics by XPEEM, J. Electron Spectrosc. Relat. Phenom. 185 (2012) 417–428, https://doi.org/10.1016/j.elspec.2012.03.002.

[49] K. Orson, Data from operando study of Ni-22Cr oxidation dynamics with nanoscale resolution in an X-ray photoemission electron microscope, Mendeley Data V1, (2024), https://doi.org/10.17632/w2p5fwc5bb.1.

[50] B.H. Frazer, B. Gilbert, B.R. Sonderegger, G. De Stasio, The probing depth of total electron yield in the sub-keV range: TEY-XAS and X-PEEM, Surf. Sci. 537 (2003) 161–167, https://doi.org/10.1016/S0039-6028(03)00613-7.

[51] J.R. Beattie, F.W.L. Esmonde-White, Exploration of principal component analysis: deriving principal component analysis visually using spectra, Appl. Spectrosc. 75 (2021) 361–375, https://doi.org/10.1177/0003702820987847.

[52] M. Lerotic, C. Jacobsen, T. Schäfer, S. Vogt, Cluster analysis of soft X-ray spectromicroscopy data, Ultramicroscopy 100 (2004) 35–57, https://doi.org/10.1016/j.ultramic.2004.01.008.

[53] R. Mak, M. Lerotic, H. Fleckenstein, S. Vogt, S.M. Wild, S. Leyffer, Y. Sheynkin, C. Jacobsen, Non-negative matrix analysis for effective feature extraction in X-ray spectromicroscopy, Faraday Discuss. 171 (2014) 357–371, https://doi.org/10.1039/c4fd00023d.

[54] D.D. Lee, H.S. Seung, Learning the parts of objects by non-negative matrix factorization, Nature 401 (1999) 788–791, https://doi.org/10.1038/44565.

[55] H. Tanimoto, X. Hongkun, M. Mizumaki, Y. Seno, J. Uchiwada, R. Yamagami, H. Kumazoe, K. Iwamitsu, Y. Kimura, K. Amezawa, I. Akai, T. Aonishi, Non-negative matrix factorization for 2D-XAS images of lithium ion batteries, J. Phys. Commun. 5 (2021) 115005, https://doi.org/10.1088/2399-6528/ac3268.

[56] M. Lerotic, R. Mak, S. Wirick, F. Meirer, C. Jacobsen, Mantis: A program for the analysis of x-ray spectromicroscopy data, J. Synchrotron Radiat. 21 (2014) 1206–1212, https://doi.org/10.1107/S1600577514013964.

[57] A.S. Hoffman, M. Greaney, J. Finzel, R. Xing, D. Covelli, V.Z. Fridman, C. Lugmair, S.R. Bare, Elucidation of puzzling questions regarding the CrOx/Al2O3 catalyst I. X-ray absorption spectroscopy aided identification of the nature of the chromium oxide species in the CrOx/Al2O3 dehydrogenation catalyst system, Appl. Catal. A Gen. 660 (2023), https://doi.org/10.1016/j.apcata.2023.119187.

[58] G.N. Parsons, Functional model for analysis of ALD nucleation and quantification of area-selective deposition, J. Vac. Sci. Technol. A 37 (2019) 020911, https://doi.org/10.1116/1.5054285.

[59] Y. Chen, C. Chen, C. Zheng, S. Dwaraknath, M.K. Horton, J. Cabana, J. Rehr, J. Vinson, A. Dozier, J.J. Kas, K.A. Persson, S.P. Ong, Database of ab initio L-edge X-ray absorption near edge structure, Sci. Data 8 (2021) 153, https://doi.org/10.1038/s41597-021-00936-5.

[60] M. Guo, E. Källman, R.V. Pinjari, R.C. Couto, L. Kragh Sørensen, R. Lindh, K. Pierloot, M. Lundberg, Fingerprinting electronic structure of heme iron by Ab initio modeling of metal L-edge X-ray absorption spectra, J. Chem. Theory Comput. 15 (2019) 477–489, https://doi.org/10.1021/acs.jctc.8b00658.

[61] Y. Suzuki, H. Hino, M. Kotsugi, K. Ono, Automated estimation of materials parameter from X-ray absorption and electron energy-loss spectra with similarity measures, NPJ Comput. Mater. 5 (2019) 39, https://doi.org/10.1038/s41524-019-0176-1.

[62] J. Schindelin, I. Arganda-Carreras, E. Frise, V. Kaynig, M. Longair, T. Pietzsch, S. Preibisch, C. Rueden, S. Saalfeld, B. Schmid, J.-Y. Tinevez, D.J. White, V. Hartenstein, K. Eliceiri, P. Tomancak, A. Cardona, Fiji: an open-source platform for biological-image analysis, Nat. Methods 9 (2012) 676–682, https://doi.org/10.1038/nmeth.2019.

[63] M.C. Biesinger, B.P. Payne, A.P. Grosvenor, L.W.M. Lau, A.R. Gerson, R.S.C. Smart, Resolving surface chemical states in XPS analysis of first row transition metals, oxides and hydroxides: Cr, Mn, Fe, Co and Ni, Appl. Surf. Sci. 257 (2011) 2717–2730, https://doi.org/10.1016/j.apsusc.2010.10.051.

[64] B.P. Payne, M.C. Biesinger, N.S. McIntyre, X-ray photoelectron spectroscopy studies of reactions on chromium metal and chromium oxide surfaces, J. Electron Spectros Relat. Phenom. 184 (2011) 29–37, https://doi.org/10.1016/j.elspec.2010.12.001.

[65] Supplemental Information Unraveling the role of W as a minor alloying element in the oxidation NiCr alloys Cameron Volders, (n.d.) 1–17.

[66] B.R. Strohmeier, An ESCA method for determining the oxide thickness on aluminum alloys, Surf. Interface Anal. 15 (1990) 51–56, https://doi.org/10.1002/sia.740150109.

[67] C. Powell, A. Jablonski, NIST Elastic Inelastic-Mean-Free-Path Database, 71, National Institute of Standards and Technology, Gaithersburg, MD, 2010. Version 1.2, SRD.

[68] Y.S. Dedkov, A.S. Vinogradov, M. Fonin, C. König, D.V. Vyalikh, A. B. Preobrajenski, S.A. Krasnikov, E.Y. Kleimenov, M.A. Nesterov, U. Rüdiger, S. L. Molodtsov, G. Güntherodt, Correlations in the electronic structure of half-metallic ferromagnetic CrO2 films: An x-ray absorption and resonant photoemission spectroscopy study, Phys. Rev. B Condens Matter Mater. Phys. 72 (2005), https://doi.org/10.1103/PhysRevB.72.060401.

[69] T. Eelbode, J. Bertels, M. Berman, D. Vandermeulen, F. Maes, R. Bisschops, M. B. Blaschko, Optimization for Medical Image Segmentation: Theory and Practice When Evaluating With Dice Score or Jaccard Index, IEEE Trans. Med Imaging 39 (2020) 3679–3690, https://doi.org/10.1109/TMI.2020.3002417.

[70] M. Rahaman, B. Johansson, A.V. Ruban, First-principles study of atomic ordering in fcc Ni-Cr alloys, Phys. Rev. B Condens Matter Mater. Phys. 89 (2014), https://doi.org/10.1103/PhysRevB.89.064103.

[71] A.L.D. Kilcoyne, D.P. Woodruff, J.E. Rowe, R.H. Gaylord, Comparative study of angle-resolved valence-band photoemission from half-monolayer structures of C, N, and O on Ni(100), Phys. Rev. B 39 (1989) 12604–12611, https://doi.org/10.1103/PhysRevB.39.12604.

[72] H. Tillborg, A. Nilsson, T. Wiell, N. Wassdahl, N. Mårtensson, J. Nordgren, Electronic structure of atomic oxygen adsorbed on Ni(100) and Cu(100) studied by soft-x-ray emission and photoelectron spectroscopies, Phys. Rev. B 47 (1993) 16464–16470, https://doi.org/10.1103/PhysRevB.47.16464.

[73] H. Nakajima, S. Pukird, W. Boonyaratgalin, T. Ishii, T. Saitoh, A. Kakizaki, Electronic and Magnetic Structures in O/Cr(001) Surface from Angle-Resolved Photoemission Spectroscopy, J. Phys. Soc. Jpn. 79 (2010) 104710, https://doi.org/10.1143/JPSJ.79.104710.

[74] A. Calloni, G. Berti, A. Brambilla, M. Riva, A. Picone, G. Bussetti, M. Finazzi, F. Ciccacci, L. Duò, Electron spectroscopy investigation of the oxidation of ultra-thin films of Ni and Cr on Fe(0 0 1), J. Phys.: Condens. Matter 26 (2014) 445001, https://doi.org/10.1088/0953-8984/26/44/445001.

[75] J.J. Yeh, I. Lindau, Atomic subshell photoionization cross sections and asymmetry parameters: $1 \leqslant Z \leqslant 103$, Data Nucl. Data Tables 32 (1985) 1–155, https://doi.org/10.1016/0092-640X(85)90016-6.

[76] V. Alexandrov, M.L. Sushko, D.K. Schreiber, S.M. Bruemmer, K.M. Rosso, Ab initio modeling of bulk and intragranular diffusion in ni alloys, J. Phys. Chem. Lett. 6 (2015) 1618–1623, https://doi.org/10.1021/acs.jpclett.5b00177.

[77] P. Simonnin, D.K. Schreiber, B.P. Uberuaga, K.M. Rosso, Atomic diffusion, segregation, and grain boundary migration in nickel-based alloys from molecular dynamics simulations, Mater. Today Commun. 35 (2023) 105768, https://doi.org/10.1016/j.mtcomm.2023.105768.

[78] M. Fanfoni, M. Tomellini, The Johnson-Mehl- Avrami-Kohnogorov model: A brief review, Il Nuovo Cim. D. 20 (1998) 1171–1182, https://doi.org/10.1007/BF03185527.

[79] K. Shirzad, C. Viney, A critical review on applications of the Avrami equation beyond materials science, J. R. Soc. Interface 20 (2023), https://doi.org/10.1098/rsif.2023.0242.

[80] T. Gheno, C. Desgranges, L. Martinelli, On the role of surface deformation in the oxidation of NiCr alloys at 340–600 °C, Corros. Sci. 173 (2020) 108805, https://doi.org/10.1016/j.corsci.2020.108805.